

## Orbital stability of ensembles of particles in regions of magnetic reconnection in Earth's magneto-tail

Christoph Lhotka,<sup>1, a)</sup> Philippe Bourdin,<sup>1, b)</sup> and Elke Pilat-Lohinger<sup>2, c)</sup>

<sup>1)</sup>*Space Research Institute, Austrian Academy of Sciences, Schmiedlstrasse 6, A-8042 Graz*

<sup>2)</sup>*Institute of Astrophysics, University of Vienna, Türkenschanzstrasse 17, A-1180 Wien*

(Dated: today)

We investigate the collective behaviour of particle orbits in the vicinity of magnetic reconnection in Earth's magneto-tail. Various regions of different kinds of orbital stability of particle motions are found. We locate regimes of temporary capture of particle orbits in configuration space as well as locations, where strong particle accelerations take place. With this study we are able to provide a detailed map, i.e. the topology, of high and low acceleration centers close to the reconnection site. Quasi-regular and chaotic kinds of motions of elementary particles can be determined as well. The orbital stability of particle orbits is obtained by a statistical analysis of the outcome of the system of variational equations of particle orbits within the framework of particle-in-cell simulations. Using the concept of Lyapunov Characteristic Numbers to ensembles of particle orbits we introduce Lyapunov Ensemble **Averages** to describe the response of particle orbits to local perturbations induced by the electro-magnetic field.

Keywords: **Lyapunov Ensemble Averages**, Magnetic reconnection, Earth magneto-tail

---

<sup>a)</sup>Electronic mail: christoph.lhotka@oeaw.ac.at

<sup>b)</sup>Electronic mail: philippe.bourdin@oeaw.ac.at

<sup>c)</sup>Electronic mail: elke.pilat-lohinger@univie.ac.at

## I. INTRODUCTION

Magnetic reconnection is a term that describes the fundamental change of connectivity within magnetic field topologies. Giovanelli<sup>13</sup> associated observations of energetic outbursts on the Sun with reconnection and several other phenomena in the Earth's magnetosphere are probably driven by reconnection, like auroral sub-storms<sup>27</sup>. While we know from Maxwell's equations that it is impossible to cut and reassemble magnetic field lines, the process of reconnection requires us to think beyond this paradigm and it is a riddle until today, what exactly happens in the micro-physical regime of reconnection. In a more macroscopic sense, established descriptions of the effects of reconnection comprise a quasi-static dissipative mechanism<sup>24,33</sup> and model with discontinuities<sup>32</sup>. After magnetic field lines reconnect, stress in the field may be released by the retraction of the newly connected field lines, which accelerates plasma together with the field and forms a slow shock within the outflow<sup>26</sup>. Fundamental reconnection physics may be studied with the help of numerical simulations and in-situ observations in space<sup>18,25,34,35</sup>. It is still difficult to reach a non-collisional regime in laboratory plasmas<sup>37,39</sup>.

When we approach the reconnection site to spatial distances of about the electron gyroradius or the current sheet thickness, we find strongly non-Maxwellian electron velocity distributions (eVDFs)<sup>4,17</sup>. We also find that there is an enhanced non-gyrotropic behavior of electrons near the stagnation point of the reconnection outflow, as well as the magnetic separatrix, which is the border between four topological distinct magnetic fields that meet in the reconnection center<sup>4</sup>. One may explain these non-gyrotropic orbits as meandering motions of electrons that cross the current sheet multiple times<sup>16,23</sup>, acceleration through electric fields<sup>3</sup>, and deflection from strongly curved magnetic fields near the reconnection center<sup>38</sup> that is also observed for ions<sup>22</sup>.

In the current study we aim to identify different kinds of behaviour of ensembles of particle orbits by means of the analysis of the system of variational equations of motion. We find regions close to the reconnection center, which support 'quasi'-regular or irregular (chaotic) kinds of orbital motions. These regions are important to better understand the mixing behaviour of particle orbits in phase space. Our results are strongly related to the study of the form of velocity distribution functions. It is clear that the structure of these distributions strongly depend on the kind of particle orbits that may cross the regions in

space, for which these distributions are calculated. Numerical and analytical studies have already been used to understand the motions of elementary particles from a dynamical systems point of view. In Buechner & Zelenyi<sup>5</sup> the ratio between the minimum radius of curvature of a magnetic field line and the maximum Larmor radius for given particle energy has been used to distinguish between regular and chaotic motion. The authors find that for ratios much larger than unity an adiabatic invariant of motion exists, while for ratios close to unity this adiabaticity breaks, and resonance overlapping between the fundamental periods of bounce- and gyromotion introduces deterministic chaos into the problem. While in Buechner & Zelenyi<sup>5</sup> the authors studied curvature alone, the combined action of field curvature and magnetic shear on the dynamics has been investigated in Buechner & Zelenyi<sup>6</sup>. A reduction of the reconnection problem to a two-degree of freedom Hamiltonian system can be found in Efthymiopoulos et al.<sup>9</sup>, but with an application to reconnection in the solar atmosphere. The authors use a perturbative approach and construct a Poincaré surface of section based on a simplified Hamiltonian model to describe various aspects of particle dynamics. The case of interactions of particles with multiple reconnecting current sheets has been investigated in Anastasiadis et al.<sup>1</sup>. In Gontikakis et al.<sup>14</sup> different kinds of orbits have been found in a 3D Harris-type reconnecting sheet where chaotic orbits lead to an escape by stochastic accelerations, regular orbits leading to escape along the field lines of the reconnecting magnetic component, and mirror-type regular orbits that are trapped on invariant tori. Analytical formulae that provide the kinetic energy gain of particle orbits are derived and validated by means of numerical simulations.

Our approach to identify the different kinds of orbital motions of particles in the vicinity of magnetic reconnection is based on the concept of Lyapunov Characteristic Exponents (LCE), see e.g.<sup>2,10</sup> which provides a quantitative estimate for chaos in case of exponential divergence of two initially nearby trajectories. As the LCE is an asymptotic quantity, which cannot be determined exactly, it is more common to use terms like LCI (Lyapunov Characteristic Indicator) or LCN (Lyapunov Characteristic Number) instead of LCE. About a decade later,<sup>7,11,12,20,28,30</sup> started to develop short-time and fast methods deduced from the LCE to distinguish between regular and chaotic motion. These methods are briefly discussed in<sup>8</sup> and more in detail in<sup>29,31</sup>.

Classical chaos indicators are defined with respect to a single orbit that obeys a unique initial condition. They are very useful tools to obtain information about the vicinity of an

orbit. Our approach differs from these classical chaos indicators as follows: our aim is to understand the collective behaviour of ensembles of particles in real space rather than the vicinity of single particle trajectories in phase space. An ensemble of particles is usually described in terms of a given velocity distribution function, which can be used to define a mean (bulk) velocity of the ensemble within a given region. In analogy we propose to generalize the concept of single particle chaos indicators and introduce the mean indicator over different particle trajectories within a given region in real space that we call Lyapunov Ensemble **Average (LEA)**. In practice we calculate the mean variation of the tangent vectors for a set of initial conditions in phase space that is confined to a given region in real space. The resulting number (**LEA**) will serve as an indicator for the given region rather than for a unique orbit, and will provide a qualitative description of the dynamics of particles trajectories that enter this specific region.

For technical reasons we require the method to be fast:

- i) Magnetic reconnection accelerates charged particles, which generates mean currents to change the electric and magnetic fields. Eventually, reconnection will end when the lowest magnetic energy state is reached. Our main interest lies in the dynamical picture of particle orbits during magnetic reconnection. The tracing of particle orbits shall end before the fields have significantly changed.
- ii) The vector fields are only given within a finite simulation box in configuration space, but numerical simulations of particle orbits show that particles may exit the box already after very short time. Therefore it is desirable to determine the indicator before the particle exits the simulation box, where the vector fields are valid, i.e. to avoid the influence of numerical errors that are more pronounced at the boundaries of the simulation boxes.

For these reasons we define a new indicator based on the finite-time approximations of LCEs, which we call Lyapunov Ensemble **Average (LEAs)**.

The mathematical set-up of the problem can be found in Sec. II, with the definition of **LEAs** in Sec. II A, and a description of the particle-in-cell (PIC) simulation data that we use in Sec. II B. The main simulation results are described in Sec. III, the conclusions and summary of our study can be found in Sec. IV.

## II. MATHEMATICAL SET-UP

Let  $q/m$  denote the charge-over-mass ratio of a particle, i.e. either electrons with  $m = m_e$  and  $q = -q_e$  or protons with  $m = m_p$  and  $q = +q_e$ , where  $q_e$  stands for elementary charge. The force of interest  $\vec{F}$ , acting on a particle of electric charge  $q$  subject to an electric and magnetic field, is given by :

$$\vec{F} = q \left( \vec{E} + \vec{v} \times \vec{B} \right) . \quad (1)$$

Here,  $\vec{E} = \vec{E}(\vec{r}, t)$  and  $\vec{B} = \vec{B}(\vec{r}, t)$  are vector fields that depend on the position of the particle  $\vec{r} = \vec{r}(t)$  at given time  $t$ ,  $\vec{v} = \vec{v}(t)$  is the velocity  $\vec{v} = d\vec{r}/dt$ , and the acceleration of the particle is simply given by:

$$\frac{d^2\vec{r}}{dt^2} = \frac{q}{m} \left( \vec{E}(\vec{r}, t) + \frac{d\vec{r}}{dt} \times \vec{B}(\vec{r}, t) \right) . \quad (2)$$

Let  $x, y, z$  and  $\dot{x}, \dot{y}, \dot{z}$  denote the components of the position and velocity vectors with  $\vec{r} = (x, y, z)$  and  $\vec{v} = (\dot{x}, \dot{y}, \dot{z})$ . To simplify the ongoing exposition we introduce the following notation: let  $(X_1, X_2, X_3)$  be the positions  $(x, y, z)$  and  $(X_4, X_5, X_6)$  be the velocities  $(\dot{x}, \dot{y}, \dot{z})$  and denote by  $\vec{X} = (X_1, \dots, X_6)$  the state vector spanned in the 6 dimensional phase space, that we denote by  $P_{\vec{X}}$  in the further discussion. In this set-up (2) can be reduced to a 6-dimensional system of first order ODEs:

$$\frac{d\vec{X}}{dt} = \vec{f}(\vec{X}, t) , \quad (3)$$

with initial conditions  $\vec{X}(0) = (X_1(0), \dots, X_6(0))$ . Here, vector function  $\vec{f} = \vec{f}(\vec{X})$ , using the notation  $\vec{F} = (F_x, F_y, F_z)$ , is given by (1) as follows:

$$\vec{f} = (X_4, X_5, X_6, F_x/m, F_y/m, F_z/m) .$$

The elements of the Jacobian matrix  $\mathbf{J} = \mathbf{J}(\vec{X})$  of (3) are given in terms of  $\vec{X}$  by:

$$\mathbf{J}_{ij} = \frac{df_i}{dX_j} , \quad i, j = 1, \dots, 6 , \quad (4)$$

where we used the notation  $\vec{f} = (f_1, \dots, f_6)$ . Let  $\vec{Y}_i$  denote the deviation vector with  $i = 1, 2, \dots, 6$ , and the matrix  $\mathbf{Y} = (\vec{Y}_1, \dots, \vec{Y}_6)$  be spanned by  $\vec{Y}_i$ . We choose  $Y_{ij}(0) = \delta_{ij}$ , with  $i, j = 1, \dots, 6$ , where  $\delta_{ij}$  denotes the Kronecker delta function with the property  $\delta_{ij} = 1$  for  $i = j$  and  $\delta_{ij} = 0$  otherwise. The evolution in time of  $\mathbf{Y} = \mathbf{Y}(t)$  is given by the linearized system of equations of motion:

$$\frac{d\mathbf{Y}}{dt} = \mathbf{J}(t)\mathbf{Y} , \quad (5)$$

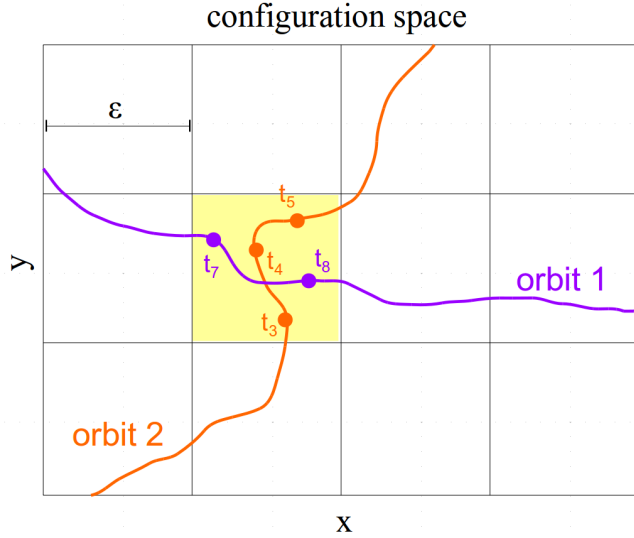


FIG. 1. Sketch of the method to calculate the **LEA**. Two orbits cross the region  $R_\varepsilon(\vec{X}_p)$  shown in yellow. Both orbits contribute with  $\Lambda_n^{(m)}$  and  $n = 7, 8$  for  $m = 1$  and  $n = 3, 4, 5$  for  $m = 2$  to the calculation of the **LEA** within the yellow cell (see text for definitions of the symbols).

with  $\mathbf{J} = \mathbf{J}(t)$  since  $\mathbf{J} = \mathbf{J}(\vec{X}(t))$ . We notice that the determination of  $\mathbf{Y}$  with respect to time  $t$  requires to solve (5) together with (3) totalling 42 ordinary equations of motion of first order in case of (1).

### A. Lyapunov Ensemble Averages

The development of the Lyapunov Ensemble **Averages** (**LEAs**) is motivated by the work of Froeschlé et al.<sup>11</sup>, Lohinger et al.<sup>20</sup>, where the authors investigate the statistical moments of the time series of the local Lyapunov Numbers. They show that the mean value of the distribution of these LLNs yield the LCE of an orbit in case  $N \rightarrow \infty$ , where  $N$  is the number of data points of LLNs for the computed time evolution of a single orbit. In Voglis & Contopoulos<sup>36</sup> the authors investigate the distribution of the so-called stretching numbers of single particle trajectories in dynamical systems. They find that the spectrum of stretching numbers is independent of the initial point along any particular orbit, that in a chaotic domain, it is independent of the initial condition, and that the mean value over the spectrum of stretching numbers tends to the LCE for  $N$  to infinity. In this study the analysis is focused on single particle trajectories. In our new approach we perform the average over

the LLNs of  $M$  particle trajectories crossing a given region instead. We provide a sketch of the method in Fig. 1. Two orbits (orbit 1, orbit 2) cross the region marked in yellow at different time stamps  $t_7, t_8$  (orbit 1) and  $t_3, t_4, t_5$  (orbit 2). The **LEA** for the yellow cell is then given by the average of the data in the two time series that correspond to these times. In practice thousands of data points per cell are used in actual calculations. The number is a mean value of possible LLNs within a given region in real space and serves as an indicator for the cell rather than for a single orbit itself.

A formal definition of the **LEA** is as follows. Let  $\Lambda = (\lambda_1, \dots, \lambda_6)$  be the spectrum of LCEs of the system (3), and  $\Lambda_n$  be the LLNs obtained at time step  $t_n$ . We denote by  $(\Lambda_n)$ , with  $n = 0, 1, \dots, N$  the time series of successive approximations of  $\Lambda$ . In the limit  $n \rightarrow \infty$  we have  $\Lambda_n \rightarrow \Lambda$  which can be approximated by the mean over  $(\Lambda_n)$  with  $n = 0, 1, \dots, N$ . To generalize the approach to multiple particle orbits we introduce the notation  $(\Lambda_n)_m$  to be the  $m$ -th time series of LLNs along the orbit of the  $m$ -th particle with  $m = 0, 1, \dots, M$ . We notice that at given time  $t_p$  ( $0 \leq p \leq N$ ) the spectrum  $\Lambda_p$  is linked to a position in phase space  $\vec{X}_p \in P_{\vec{X}}$  since  $\mathbf{J}$  in (4) also depends on  $\vec{X}$ . Let  $R_\varepsilon(\vec{X}_p) \subset P_{\vec{X}}$  be the  $\varepsilon$ -region centered around  $\vec{X}_p$ :

$$R_\varepsilon(\vec{X}_p) = \{\vec{X} : \|\vec{X} - \vec{X}_p\| \leq \varepsilon\} .$$

Let  $(\Lambda_n)_m = (\Lambda_0^{(m)}, \Lambda_1^{(m)}, \dots, \Lambda_N^{(m)})$ , and  $\Lambda_n^{(m)}$  be the  $n$ -th element of the  $m$ -th time series of LLNs. We define the set  $\mathcal{M}_p^\varepsilon$  of  $\Lambda_n^{(m)}$  passing through  $R_\varepsilon(\vec{X}_p)$  as follows:

$$\mathcal{M}_p^\varepsilon = \{\Lambda_n^{(m)} : \vec{X}_n \subset R_\varepsilon(\vec{X}_p)\} .$$

Within this context the spectrum of **LEAs** associated to a given point  $\vec{X}_p$  is given by the mean values over all elements that belong to  $\mathcal{M}_p^\varepsilon$ :

$$\bar{\Lambda}_{p,\varepsilon} = \mu(\mathcal{M}_p^\varepsilon) . \quad (6)$$

We notice that  $\bar{\Lambda}_{p,\varepsilon}$  defined in terms of (6) defines a spectrum in an  $\varepsilon$ -region around  $\vec{X}_p \in P_{\vec{X}}$ . In the limit  $\varepsilon \rightarrow 0$  the quantity  $\bar{\Lambda}_{p,\varepsilon}$  reduces to the instant value  $\Lambda_p$  at given location  $\vec{X}_p \in P_{\vec{X}}$  at time  $t_p$  since  $\vec{X}_p = \vec{X}(t_p)$  and by the existence and uniqueness theorem of ordinary equations of motion. To ensure that enough data points cross  $R_\varepsilon(\vec{X}_p)$  small quantity  $\varepsilon$  has to be chosen large enough. In the following, for the sake of simplicity in the notation, we will denote by  $\bar{\Lambda} = (\bar{\lambda}_1, \dots, \bar{\lambda}_6)$  the **LEA** for any point  $\vec{X}_p \in P_{\vec{X}}$  and for fixed value  $\varepsilon = \varepsilon^*$  with  $\varepsilon^* > 0$ .

## B. Numerical Simulation setup

The electric and magnetic fields in (1) are obtained from a PIC simulation of anti-parallel magnetic fields using the open-source code "iPic3D"<sup>21</sup>. We use the simulation data from<sup>4</sup>, which provides a catalog of detailed electron velocity distribution functions that are comparable with in-situ observations of electrons in the tail of Earth's magnetosphere.

The PIC model is a two-dimensional (2D) setup that represents a reconnection region in the magneto-tail of Earth, as well as certain magnetic field configurations on the Sun. The anti-parallel field lies within the plane of the simulation, where the  $x$ -coordinate is parallel to the initial background magnetic field  $B_0 = 0.05477$ . We allow the particle position vectors, particle velocity vectors, and the field vectors to have an out-of-plane component, which is often called a 2.5D setup. Our physical domain spans over  $25.6 \times 12.8 d_i^2$  which we cover with  $512 \times 256$  grid cells. The ion inertial length  $d_i$  defines our characteristic length scale and is set by  $B_0$  together with the initial background number density  $n_0 = 0.2$ . Our computational grid distance is hence  $\Delta r = 0.05 d_i$  and we fill each 3D grid cell with  $2^{15}$  particles of each species, electrons and protons.

We execute the simulation run on our in-house *LEO* computing cluster in Graz, where we require a minimum of 8 compute nodes with 128 processors in parallel and about 1.5 TB of RAM in total for about 16 hrs.

The initial magnetic field and average particle velocities follow an analytical Harris current sheet solution<sup>15</sup> that is supposed to remain stable. To trigger the reconnection exactly in the middle of the simulation domain, we add a small perturbation to the initial fields. Unlike earlier works, our perturbation is much smaller in amplitude and spatial extent and hence the evolution of the reconnection becomes more self-consistent<sup>4</sup>. We observe a free evolution of the reconnection until about  $t = 22 \Omega_i^{-1}$ , where  $\Omega_i = e B_0 / m_p$  is the ion gyrofrequency,  $e$  is the charge of a proton, and  $m_p$  is its mass. Therefore, we take the magnetic field data from a snapshot near  $t_c = 20.54 \Omega_i^{-1}$ , when the reconnection is well developed but still in its free evolution phase. The high-cadence magnetic and electric field data that we obtain from our PIC simulation allows us to propagate particles in a realistic way with time-interpolated field information.

For this study, we use ensembles of test particles that we propagate outside of the main PIC simulation code, so that we are able to propagate also the equation systems (3) and



(5). As our main PIC simulation run has a very large number of particles, we do have an unprecedented low noise level in our magnetic and electric fields,  $\vec{B}$  and  $\vec{E}$ .

The vector fields  $\vec{E}(\vec{r}, t)$  and  $\vec{B}(\vec{r}, t)$  that enter (1) are given from the PIC simulations on a discrete grid ( $\vec{r}_i, t_i$  with index  $i$ ) only. Let  $I_x = (-L_x, L_x)$ ,  $I_y = (-L_y, L_y)$ , and  $I_z = (-L_z, L_z)$  denote three intervals with limits  $L_x$ ,  $L_y$ , and  $L_z$  (with  $L_x = -12.8d_i$ ,  $L_y = 6.4d_i$ ,  $L_z = 0.5d_i$  in normalized units). The fields are defined within  $I = I_x \times I_y \times I_z$  on equally spaced points with spacings  $\Delta x$ ,  $\Delta y$ , and  $\Delta z$  equal  $0.05d_i$ . We use linear interpolation between the grid points on the space  $I_x \times I_y$  and constant periodic interpolation within the interval  $I_z$  to calculate  $\vec{E}(\vec{r}, t)$  and  $\vec{B}(\vec{r}, t)$  for any given point in  $I$  with  $|x| \leq L_x$ ,  $|y| \leq L_y$ . We notice that the interpolation routines use divided differences to construct Lagrange or Hermite interpolating polynomials. For the variational system (5) it also requires to evaluate first order derivatives of the vector fields  $\vec{E}$  and  $\vec{B}$ , i.e.  $d\vec{E}(\vec{r}, t)/dx$ ,  $d\vec{E}(\vec{r}, t)/dy$ , and  $d\vec{E}(\vec{r}, t)/dz$ , as well as  $d\vec{B}(\vec{r}, t)/dx$ ,  $d\vec{B}(\vec{r}, t)/dy$ , and  $d\vec{B}(\vec{r}, t)/dz$ . The derivatives are calculated by piecewise symbolic differentiation of the interpolating polynomials instead of the difference quotient rule.

We fix the vector fields with respect to time  $t$  in the following discussion. The approximation is valid since the time that single particle orbits need to cross the simulation domain is much shorter than the timescales on which the electric and magnetic fields change. For the sake of simplicity we use the notation  $\vec{E}(x, y, z) = \vec{E}(x, y, z, t_c)$  and  $\vec{B}(x, y, z) = \vec{B}(x, y, z, t_c)$  from now on. The interpolated vector fields are shown in Fig. 2. Fields have been normalized by the background field strength  $B_0$ , and the maximum electric field strength  $E_0$ . A comparison of our vector field with a Harris type reconnecting current sheet model<sup>19</sup> is shown in Fig. 3. The plot shows the quantity  $B_x(y) = B_x(0, y, 0)$  in the interval  $I_y$ . The dashed line corresponds to a Harris type approximation of the component  $B_x(y)$ . It perfectly agrees with the vector field close to the reconnection center (gray-shaded region), while away from the center the analytical model only qualitatively reproduces the results. We remark, that in simplified models the electric vector field is usually approximated by a constant  $E_0$ , i.e. by  $\vec{E} = (0, 0, E_0)$ , which is valid in comparison with the component  $E_z$  in Fig. 2. However, in the other components, we clearly see that a sign change, e.g. in  $E_y(y) = E(x = 0, y, z = 0)$ , has to be taken into account for changing sign in  $y$ .

The system of differential equations (3) and (5) is solved in Wolfram Mathematica (Version 11) using the NDSolve framework using ExplicitRungeKutta method with difference

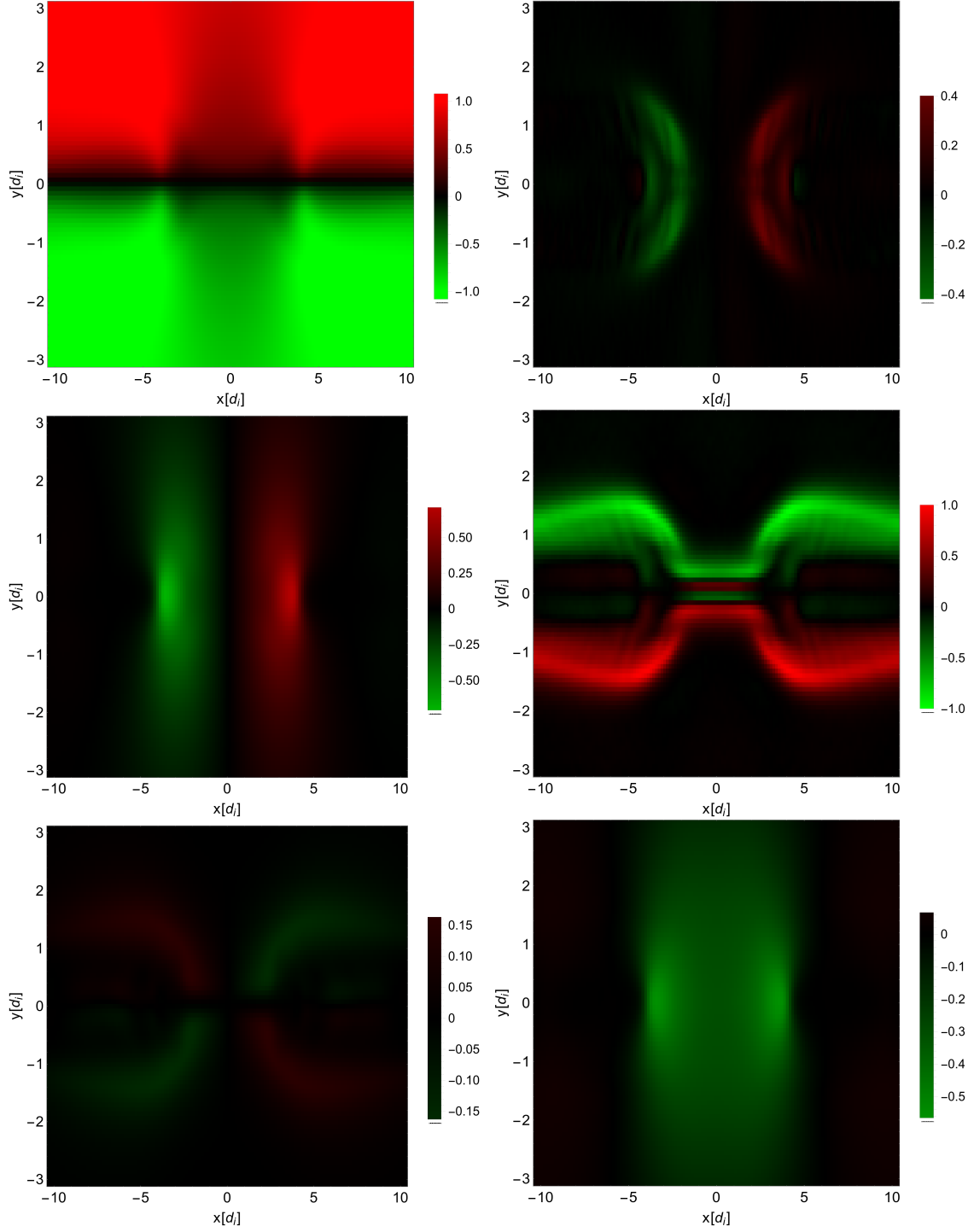


FIG. 2. Normalized components  $x$  (top),  $y$  (middle), and  $z$  (bottom) of vector field  $\vec{B}$  (left column) and  $\vec{E}$  (right column), respectively.

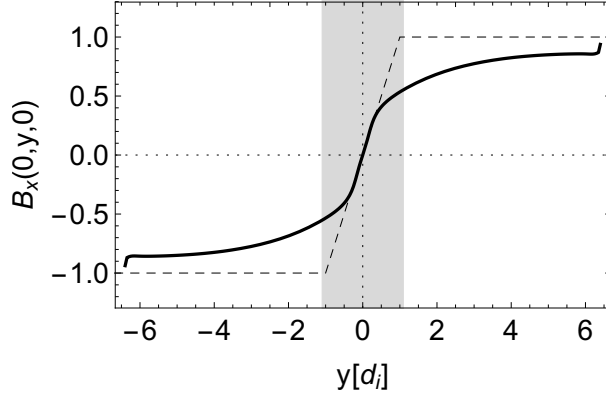


FIG. 3. Normalized  $B_x(0, y, 0)$  component of the magnetic field  $\vec{B}$  versus  $y$ . Dashed lines correspond to a Harris type model, see text.

order 8 and variable step size control. The numerical integrator has been adapted to incorporate the calculation of the **LEAs** at given time steps,  $\Delta t = 0.1$ , of the numerical integration by direct access to the NDSolve data structures. The initial conditions are taken within the region  $x(0) \in (0, 10)d_i$  and  $y(0) \in (0, 5)d_i$  with  $z(0) = 0d_i$  and initial velocities  $\dot{x}(0)$ ,  $\dot{y}(0)$  are obtained from a two-dimensional Maxwellian distribution, while  $\dot{z}(0)$  is taken to be zero for all initial conditions. The initial deviation vectors  $\vec{Y}_i$  for each initial condition  $\vec{X}(0)$  are taken to be  $Y_{ij}(0) = \delta_{ij}$ ,  $i, j = 1, \dots, 6$  (see Sec. II). After each time step  $n\Delta t$ , with  $\Delta t = 0.1$  an orthogonal basis  $\vec{Y}_i^*(n\Delta t)$  is obtained from  $\vec{Y}_i(n\Delta t)$  by means of a Gram-Schmidt orthogonalization process. The spectra  $(\Lambda_n)$  are then calculated from the norm of the projections of  $\vec{Y}_i(n\Delta t)$  onto  $\vec{Y}_i^*(n\Delta t)$ , which is also used as the new initial condition to continue the integration of (5). The resulting time series  $(\vec{\Lambda}_n)_m$  serve as the basis for the calculation of the **LEAs** as outlined in Sec II. Integration is stopped either when the particle leaves the rectangular region  $|L_x| \times |L_y|$  or when the integration time exceeds the limit where the approximations of the vector fields  $\vec{E}$ ,  $\vec{B}$  are not valid anymore.

The accuracy of the methodology relies on the accuracy of the vector fields  $\vec{B}$ ,  $\vec{E}$  that have been obtained from PIC simulations with a very high number of particles and a low noise in the electric fields. We do see fluctuations in the electric fields of the order of  $10^{-5}$ , that are due to the finite number of particles that have been used per grid cell. The total energy in our PIC simulations is conserved with a precision of 0.18%. We also checked that the dominant component of the magnetic field  $B_x(0, y, 0)$  is in agreement with a Harris type model (see

Fig. 3). To estimate the numerical error of the vector fields and their partial derivatives with respect to  $x$ ,  $y$ ,  $z$ , we took the magnitude of the non-zero value of the divergence of the vector field  $|\nabla \cdot \vec{B}| \simeq 10^{-5}$  evaluated at the reconnection center  $x = y = z = 0$ . For the numerical integration of (3) and (5) the precision of the integration method was set to  $10^{-10}$ , which is still double the orders of magnitude than the calculated error of the vector field at the reconnection center. We notice that the design of the **LEA** method does not require long-term simulations of individual particle trajectories if one ensures that enough particles are taken into account in the averaging process. The numerical errors in the integration will therefore not grow too much as long as we set the maximum time of integration small enough, which is true in our case, since it is limited by the fact that the electrons exit the PIC simulation box already after short time.

### III. NUMERICAL SIMULATIONS AND RESULTS

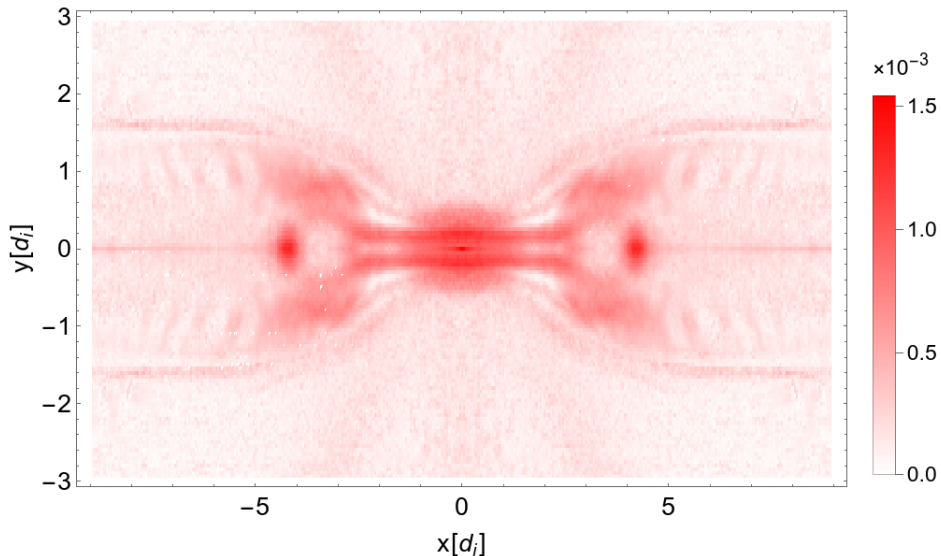


FIG. 4. Maximum **LEA** number  $\bar{\Lambda}_{max}$  projected to the space  $I_x \times I_y$ .

Our results are given in terms of the spectrum  $\bar{\lambda}_1, \dots, \bar{\lambda}_6$ . In the following we investigate different quantities derived on the basis of this complete set of **LEAs**. We first investigate the quantity  $\bar{\Lambda}_{max} = \max_{i=1, \dots, 6} \bar{\lambda}_i$  which serves as an indicator for the overall stretching / contracting behaviour of ensemble of particles. This number is shown in color code for different cells with  $\Delta x = \Delta y = 0.05d_i$ , and projected to the  $(x, y)$ -plane in Fig. 4. We

clearly see that  $\bar{\Lambda}_{max}$  is positive or zero throughout ( $I_x \times I_y$ ). This indicates that on the mean particles within ensembles experience divergence and growth of local perturbations throughout the reconnection center with high probability. Still, the strength of growth is not uniform. We find regions of variable magnitudes in  $\bar{\Lambda}_{max}$  with peaks at various places, i.e. at the reconnection center or around the island located at about  $x = 4.5d_i$ ,  $y = 0d_i$ . In other regimes  $\bar{\Lambda}_{max}$  is fluctuating, e.g. within the region inside the separatrix, or the central inflow regime.

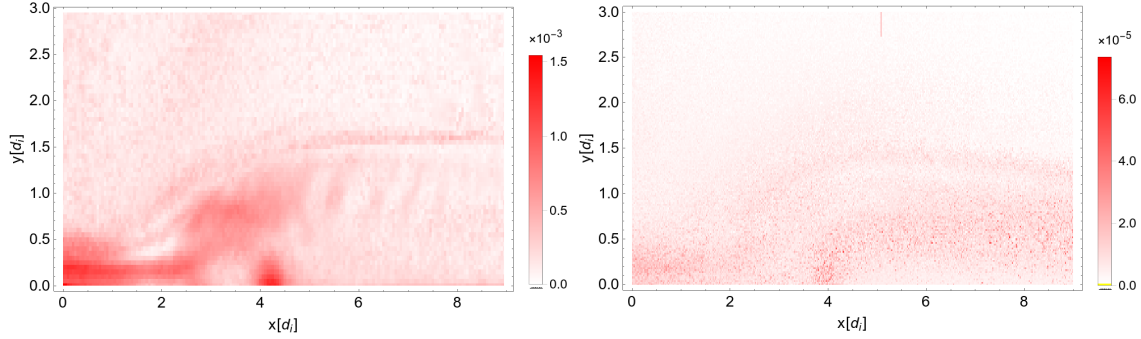


FIG. 5. Comparison of **LEA** (left) with **FLI** (right).

**Our first test in this work is to check the similarity of the LEA with the original Fast Lyapunov Indicator (FLI, Froeschlé<sup>10</sup>) in Fig. 5.** The left panel shows a magnification of the upper right part of Fig. 4 and the right panel displays the FLI results based on the same data set. The comparison of both figures clearly shows that the most pronounced features are visible in both plots, but are less visible in the FLI figure, which can be explained by the fact that the FLI is calculated for a single trajectory while the **LEA** is a statistical quantity derived on the basis of multiple orbits. **We notice that this test may be incomplete, because the FLI is not based on local ensemble averages, like our LEA method is. Therefore, future work should use several chaos indicators<sup>29,31</sup>, like GALI, FLI, MEGNO, RLI, and SALI, averaged locally in the same way as our LEA approach.** Fig. 4 should also be compared with the panels of Fig. 2 of Bourdin<sup>4</sup> (we remark, that the coordinates  $y$  and  $z$  need to be exchanged for the comparison). First, we clearly observe that the locations of the main features of Fig. 4 are also present in Bourdin<sup>4</sup>. Most visible the reconnection electric field (panel c)) is strongest in magnitudes at locations, where the dark red regions appear in Fig. 4. We conclude, that

the effect of the perturbations due to the reconnection electric field is most efficient on ensembles of particle orbits, where the **LEAs** peaks in Fig. 4. The consequence of these findings on the dynamics of ensembles of particle orbits is as follows: in dark red regimes strong accelerations take place and lead to an increase of local perturbations in magnitudes, which then results in changes in the evolution of individual orbits (see also show cases at the end of this section). On the contrary, perturbations in light red to white regions of the space  $(x, y)$  are less effective.

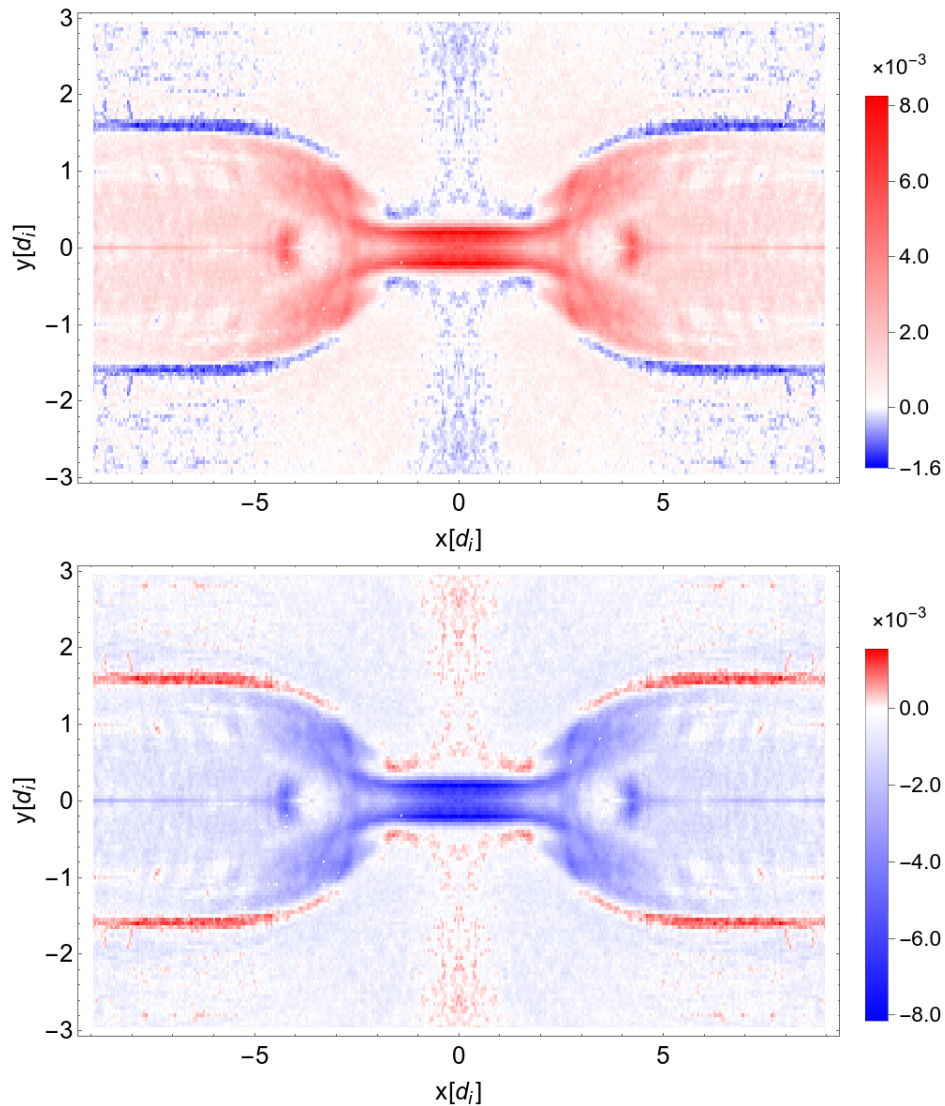


FIG. 6. Comparison of the quantity  $\bar{\Lambda}_{123}$  (top) and the quantity  $\bar{\Lambda}_{456}$  (bottom) projected to the space  $I_x \times I_y$ .

In Fig. 6 we compare the average over  $\bar{\lambda}_i$  with  $i = 1, 2, 3$  ( $\bar{\Lambda}_{123}$ ) with the average over  $\bar{\lambda}_i$

with  $i = 4, 5, 6$  ( $\bar{\Lambda}_{456}$ ) provided in color scale in the space  $I_x \times I_y$ . Here, the index  $i$  refers to the initial deviation vector  $Y_i$ , with  $i = 1, 2, \dots, 6$ . Negative values are shown in blue and correspond to  $\bar{\Lambda}_{123}$  ( $\bar{\Lambda}_{456}$ ) smaller than unity while the quantities larger than unity are shown in red. We clearly see the complementary character of the two quantities: each region in red (blue) in the upper figure has its correspondence in blue (red) in the bottom one. The symmetry is due to the coupling of the generalized variables  $\vec{X}(0)$  and the symmetric choice of the initial deviation vectors  $\vec{Y}(0)$ . A comparison of  $\bar{\Lambda}_{max}$ ,  $\bar{\Lambda}_{123}$ , and  $\bar{\Lambda}_{456}$  is shown in Fig. 7. Notice the antisymmetry between  $\bar{\Lambda}_{123}$  and  $\bar{\Lambda}_{456}$  due to the symplectic structure of the dynamical problem.

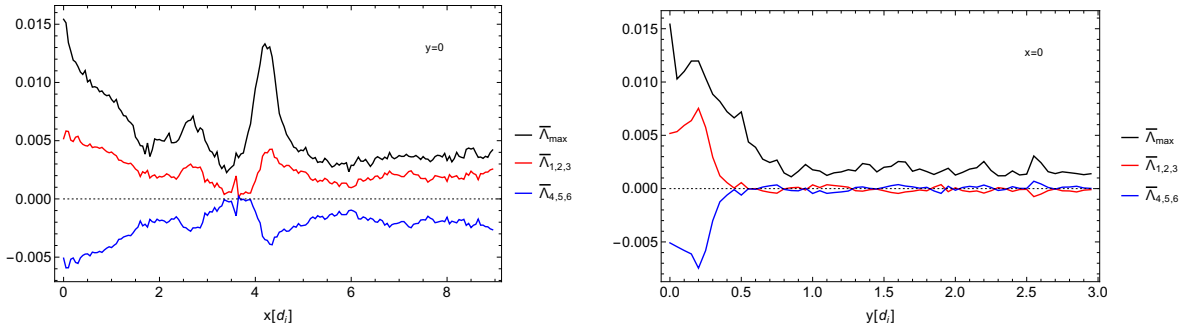


FIG. 7.  $\bar{\Lambda}_{max}$ ,  $\bar{\Lambda}_{123}$ , and  $\bar{\Lambda}_{456}$  for  $y = 0$  (left), and  $x = 0$  (right), respectively.

In classical theory the LCE and derived quantities are mainly used to distinguish between regular and chaotic motions of individual particles in phase space. In the present study we rather intend to use the **LEA** to characterize the mean influence of local perturbations on ensembles of particle orbits at different locations close to the reconnection center. To demonstrate the usefulness of the approach we show typical particle trajectories in Fig 8–10. In these figures, specific orbits are projected to the  $(x, y)$ -plane, and as well as onto specific phase planes  $(x, v_x)$ ,  $(y, v_y)$ , and  $(z, v_z)$ , respectively. The color codes in the projections are the same as in Figs. 4-6. In projections to phase planes (e.g.  $x-v_x$  in Fig. 8 and  $y-v_y$ ,  $z-v_z$  in Fig. 9) the color code indicates the local values of the **LEA** at given position of the particle orbit in the space  $(x, y)$ . As an example, the dark spot in the left panel of Fig. 8 corresponds to the dark stripe in the right panel of the same figure. Test particles are started with zero velocity at given location in the  $(x, y)$ -plane. A case with large positive value of the maximum **LEA** is shown in Fig. 8. The projection of the orbit onto the  $(x, y)$ -plane shows that the orbit crosses a dark red spot located at  $x \simeq 4.2d_i$  and  $y \simeq 0d_i$  just after

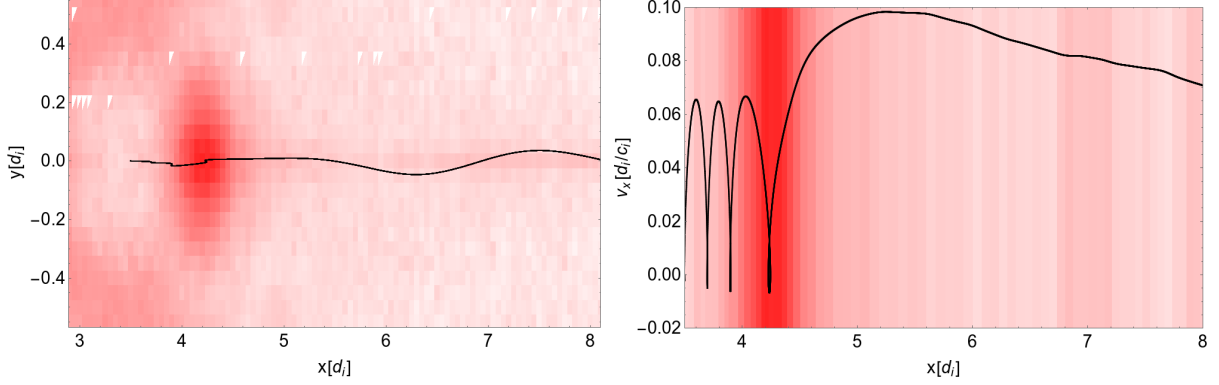


FIG. 8. Particle orbit (black) starting with zero velocity and  $y = 0d_i$  at  $x(0) = 3.5d_i$ . Left: projection of the orbit to the  $(x, y)$ -plane; right: projection to  $(x, v_x)$  (background shows maximum **LEA**, the color code is the same as in Fig. 4).

its initial release at  $x(0) = 3.5d_i$ . The effect of the crossing on the shape of the orbit in phase space becomes clear when looking on the projection of the orbit on the  $(x, v_x)$ -plane. While in the light red region on the left of the spot / stripe the drift along the  $x$ -direction is small, and regular kind of oscillations along the velocity direction takes place, accelerations along the  $x$ -direction strongly increases when the particle enters the dark red spot. The effect completely destroys the oscillatory behaviour in the  $(x, v_x)$ -plane, and drift in the  $x$  direction becomes dominant. After exiting the spot / stripe the effect of the perturbation becomes less efficient, and the particle loses its velocity component along the  $v_x$  direction, before exiting the simulation box.

An example of the effect of negative values of the **LEA** on particle orbits is shown in Fig. 9. The orbit stays in the vicinity of its initial release, but with increasing values in  $z$ . Motion takes place on quasi-periodic curves in the  $(x, v_x)$ - and  $(y, v_y)$ -planes. As a result, the orbit is trapped in rectangular region in its projection to the  $(x, y)$ -plane, a phenomenon which is known to exist in plasma physics and called 'magnetic bottle'.

We notice that orbits shown in Fig. 8 and Fig. 9 have carefully been chosen to explain the effect of positive/negative values of the **LEA** on the evolution of particle orbits. In our examples, the initial velocity and out-of-plane direction have been set to zero for demonstration purpose only. It is clear that different orbits entering red or blue labeled cells close to the reconnection center will behave differently, i.e. experience different kinds of accelerations depending on their actual dynamical state when crossing the regions. Typical examples of



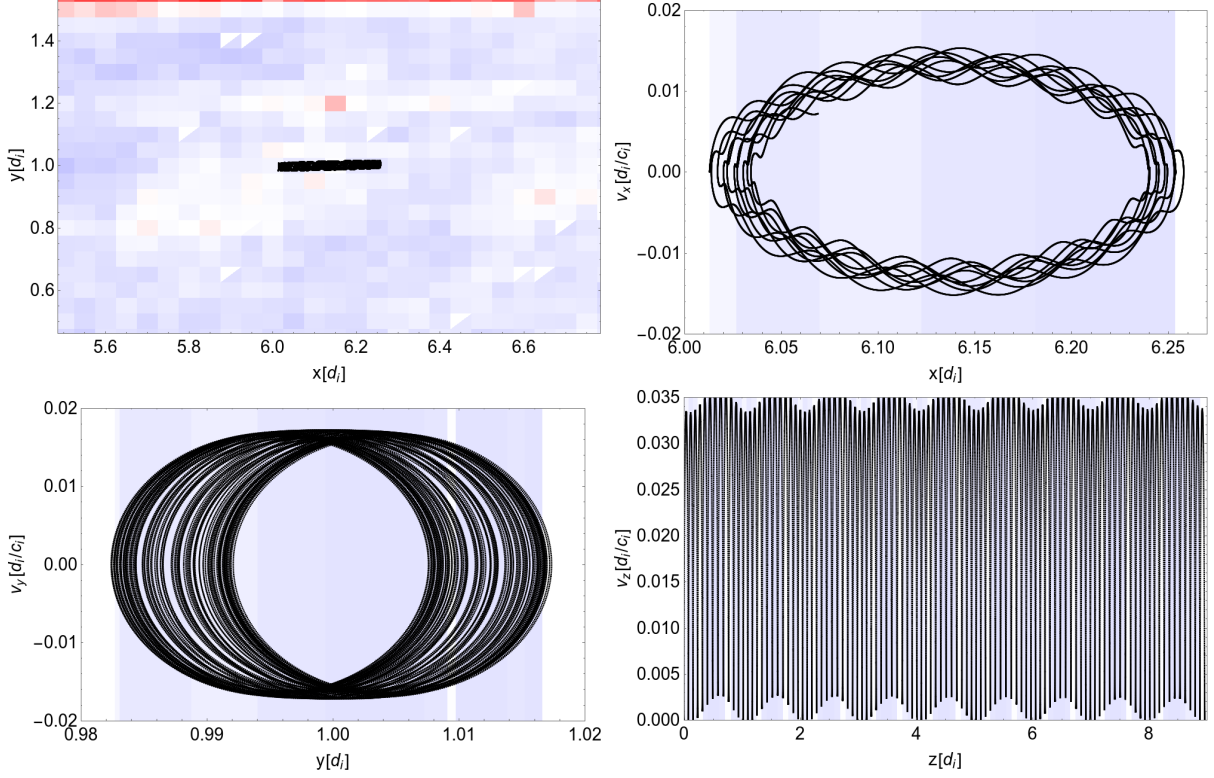


FIG. 9. Particle orbit (black) starting with zero velocity at  $x(0) \simeq 6.013d_i$  and  $y(0) \simeq 0.983d_i$ . Projection to the  $(x, y)$  (upper left),  $(x, v_x)$  (upper right),  $(y, v_y)$  (lower left), and  $(z, v_z)$ -planes, respectively. The background shows average of **LEA** over velocity directions, the color code is the same as in Fig. 6.

such orbits are shown in Fig. 10. In both cases, the particle orbits enter regions with **LEAs** of opposite sign. The darker the red regions and the stronger the magnitudes of the **LEAs**, the stronger is the accelerations along the  $x$  ( $y$ ) directions. In regions with smaller magnitudes, the drift in  $x$  ( $y$ ) directions is reduced, and oscillatory behaviour along the  $v_x$  ( $v_y$ ) planes takes place. The role of dark blue regions (related to negative values of **LEAs**) is to reduce drift along the  $x$  ( $y$ ) directions and to support oscillatory kind of behaviour of the orbit. As a direct consequence orbits remain longer in regions of magnetic reconnection which can be associated to negative values of the **LEA**. We remark that we started this study using classical methods, e.g. the classical maximum Lyapunov Exponent method (mLE). The results were unsatisfactory, and difficult to interpret for the following reason: while some classical chaos indicators showed stable kinds of motion, individual particle tra-

jectories did not stay in the vicinity of its initial condition. Also, particle trajectories were confined to regions in phase space for long time while the chaos indicator predicted them to be unstable. This phenomenon can easily be explained when looking at the lower right of Fig. 10: the orbit shown in black stays the majority of its integration time close to its initial condition and performing quasi-periodic kinds of oscillations. Eventually, the orbit escapes to the left and exits the simulation box already after very short time. A classical chaos indicator would render the orbit to be unstable if one would calculate, e.g. the mLE on the basis of the whole orbit. But, the same indicator would render the orbit to be stable if one would exclude the last part of the orbit. The solution to the problem is the **LEA**: the color code in Fig. 10 clearly demonstrates that the single orbit behaves regular within the blue region, while it behaves chaotic in the red region.

#### IV. SUMMARY & DISCUSSIONS

Particle orbits in the vicinity of regimes of magnetic reconnection are subject to concurrent magnetic and electric perturbations of different origins. It is a natural step to investigate the effect of these kinds of perturbations on particle orbits using tools of nonlinear dynamics. In classical nonlinear problems, Lyapunov Characteristic Exponents have shown to be a useful tool to distinguish between regular and chaotic kinds of motion in phase space. The exponents are based on the concept of tangent space, i.e. on the variational equations of the dynamical system in mind. In this work we study the dynamical problem of particle orbits in regimes of magnetic reconnection in Earth's magneto-tail. We are interested in the effect of different magnetic topologies on the change of the geometry of particle orbits in different regions of magnetic reconnection. For this reason we derive and make use of the system of variational equations that govern the evolution of particle orbits in phase space. Our particle simulations are based on electric and magnetic fields that have been obtained using PIC simulations. Next, we generalize the concept of LEs to ensembles of particles, and introduce the Lyapunov Ensemble **Averages**. This quantity serves as a useful tool to distinguish between regions of fast and slow accelerations along different directions in phase space, in particular to locate regions of oscillatory orbits and 'quasi'-regular kinds of motion. It is possible to define regions in phase and configuration space, where ensembles of particle orbits are trapped for much longer times with respect to regions indicating strong

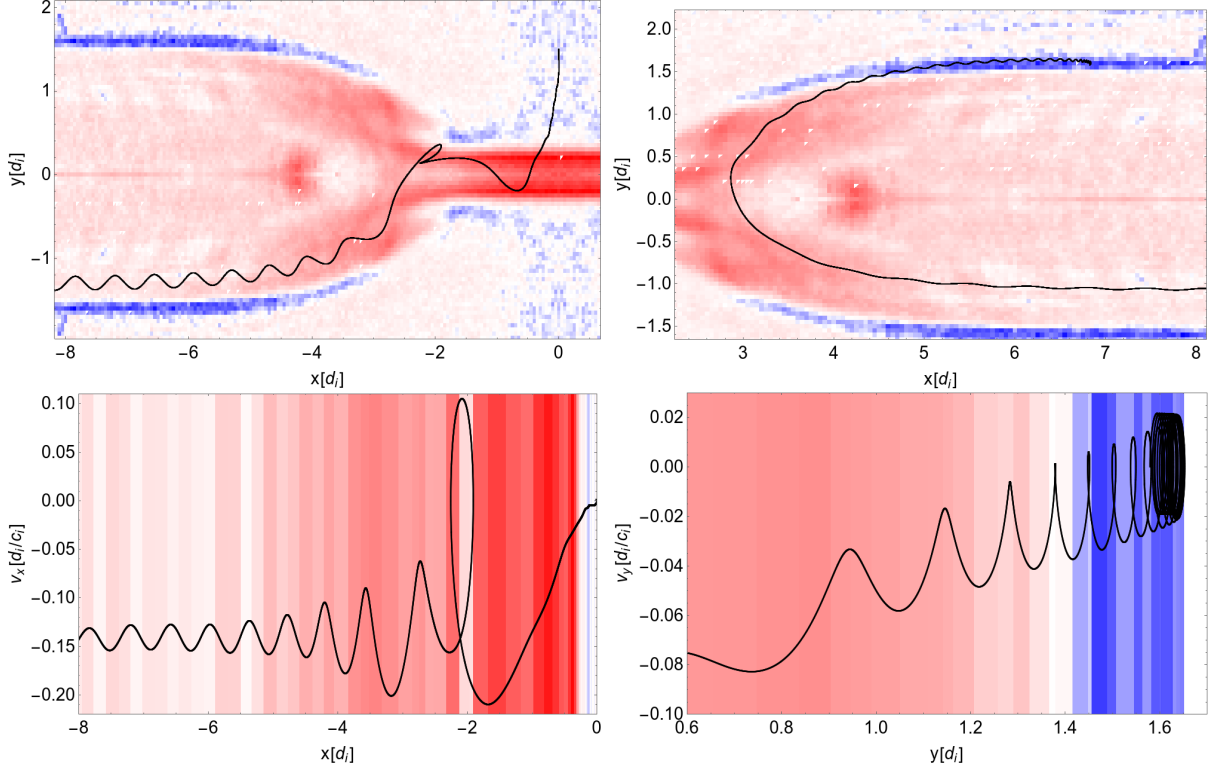


FIG. 10. Two distinct particle orbits that cross different regions of **LEAs**. Left: orbit starting at  $x(0) = 0d_i$ ,  $y(0) = 1.5d_i$  within the central inflow region; projection to the  $(x, y)$ -plane (top, left) and projection to the  $(x, v_x)$ -plane (bottom, left). Right: orbit starting at  $x(0) = 6.826d_i$  and  $y(0) = 1.580d_i$  at the border of the separatrix; projection to the  $(x, y)$  (top, right) and  $(y, v_y)$  (bottom, right) planes, respectively. Background shows average of **LEA** over position space the color code is the same as in Fig. 6.

accelerations.

Our study is a first in a series of studies related to the problem of magnetic reconnection from a dynamical systems point of view. In our ongoing study we investigate different magnetic field configurations by the means of **LEA** methods, and the possibility to derive additional macroscopic observables on the basis of the **LEAs**. Our results may also serve for a better interpretation of observations from space measurements in Earth's magneto-tail, e.g. the Cluster, Themis, MMS and other mission.

## ACKNOWLEDGEMENTS

This work took benefit from the FWF project P30542-N27 (CL), and FWF project FWF S11608-N16 (EPL). We gratefully thank the plasma group at the Space Research Institute for fruitful discussions, i.e. R. Nakamura, T. Nakamura, Y. Narita, Y.L. Sasunov, and Z. Vörös. We thank an anonymous reviewer for critical comments during the peer-reviewing process.

## REFERENCES

- <sup>1</sup>Anastasiadis, A., Gontikakis, C., & Efthymiopoulos, C. 2008, *Solar Physics*, 253, 199
- <sup>2</sup>Benettin, G., Galgani, L., Giorgilli, A., & Strelcyn, J.-M. 1980, *Meccanica*, 15, 9
- <sup>3</sup>Bessho, N., Chen, L.-J., Shuster, J. R., & Wang, S. 2014, *Geophys. Res. Lett.*, 41, 8688
- <sup>4</sup>Bourdin, P.-A. 2017, *An. Geo.*, 35, 1051
- <sup>5</sup>Buechner, J., & Zelenyi, L. M. 1989, *Journal of Geophysical Research*, 94, 11821
- <sup>6</sup>—. 1991, *Advances in Space Research*, 11, 177
- <sup>7</sup>Contopoulos, G., & Voglis, N. 1996, *Celestial Mechanics and Dynamical Astronomy*, 64, 1
- <sup>8</sup>Dvorak, R., & Lhotka, C. 2013, *Celestial Dynamics: Chaoticity and Dynamics of Celestial Systems* (Wiley)
- <sup>9</sup>Efthymiopoulos, C., Gontikakis, C., & Anastasiadis, A. 2005, *Astronomy and Astrophysics*, 443, 663
- <sup>10</sup>Froeschlé, C. 1984, *Journal de Mecanique Theorique et Appliquee Supplement*, 101
- <sup>11</sup>Froeschlé, C., Froeschlé, C., & Lohinger, E. 1993, *Celestial Mechanics and Dynamical Astronomy*, 56, 307
- <sup>12</sup>Froeschlé, C., Lega, E., & Gonczi, R. 1997, *Celestial Mechanics and Dynamical Astronomy*, 67, 41
- <sup>13</sup>Giovanelli, R. G. 1946, *Nature*, 158, 81
- <sup>14</sup>Gontikakis, C., Efthymiopoulos, C., & Anastasiadis, A. 2006, *MNRAS*, 368, 293
- <sup>15</sup>Harris, E. G. 1962, *Il Nuovo Cimento*, 23, 115
- <sup>16</sup>Horiuchi, R., & Sato, T. 1994, *Phys. Plasmas*, 1, 3587
- <sup>17</sup>Hoshino, M., Hiraide, K., & Mukai, T. 2001, *Earth Planets & Space*, 53, 627

- <sup>18</sup>Karimabadi, H., Roytershteyn, V., Daughton, W., & Liu, Y.-H. 2013, *Space Sci. Rev.*, 178, 307
- <sup>19</sup>Litvinenko, Y. E., & Somov, B. V. 1993, *Solar Physics*, 146, 127
- <sup>20</sup>Lohinger, E., Froeschlé, C., & Dvorak, R. 1993, *Celestial Mechanics and Dynamical Astronomy*, 56, 315
- <sup>21</sup>Markidis, S., Lapenta, G., & Rizwan-uddin. 2010, *Mathematics and Computers in Simulation*, 80, 1509 , multiscale modeling of moving interfaces in materials
- <sup>22</sup>Nagai, T., Shinohara, I., & Zenitani, S. 2015, *J. Geophys. Res.: Space Phys.*, 120, 1766
- <sup>23</sup>Ng, J., Egedal, J., Le, A., & Daughton, W. 2012, *Phys. Plasmas*, 19, 112108
- <sup>24</sup>Parker, E. N. 1957, *J. Geophys. Res.*, 62, 509
- <sup>25</sup>Paschmann, G., Øieroset, M., & Phan, T. 2013, *Space Sci. Rev.*, 178, 385
- <sup>26</sup>Petschek, A. G. 1964, *J. Geophys. Res.*, 69, 1428
- <sup>27</sup>Russell, C. T., & McPherron, R. L. 1973, *Space Sci. Rev.*, 15, 205
- <sup>28</sup>Sándor, Z., Érdi, B., Széll, A., & Funk, B. 2004, *Celestial Mechanics and Dynamical Astronomy*, 90, 127
- <sup>29</sup>Skokos, C. 2010, in *Lecture Notes in Physics*, Berlin Springer Verlag, Vol. 790, Lecture Notes in Physics, Berlin Springer Verlag, ed. J. Souchay & R. Dvorak, 63–135
- <sup>30</sup>Skokos, C., Bountis, T. C., & Antonopoulos, C. 2007, *Physica D Nonlinear Phenomena*, 231, 30
- <sup>31</sup>Skokos, C., Gottwald, G., & Laskar, J. 2016, *Chaos Detection and Predictability*, Lecture Notes in Physics (Springer Berlin Heidelberg)
- <sup>32</sup>Sonnerup, B. U. Ö. 1970, *J. Plasma Phys.*, 4, 161
- <sup>33</sup>Sweet, P. A. 1958, in *IAU Symposium*, Vol. 6, *Electromagnetic Phenomena in Cosmical Physics*, ed. B. Lehnert, 123–134
- <sup>34</sup>Treumann, R. A., & Baumjohann, W. 2013, *Front. Phys.*, 1, 31
- <sup>35</sup>—. 2015, *A&A Rev.*, 23, 4
- <sup>36</sup>Voglis, N., & Contopoulos, G. J. 1994, *Journal of Physics A Mathematical General*, 27, 4899
- <sup>37</sup>Yamada, M., Kulsrud, R., & Ji, H. 2010, *Rev. Modern Phys.*, 82, 603
- <sup>38</sup>Zenitani, S., & Nagai, T. 2016, *Phys. Plasmas*, 23, 102102
- <sup>39</sup>Zweibel, E. G., & Yamada, M. 2009, *ARA&A*, 47, 291